

# Preparations and Electrostatic Modelling of a Short-Range Test of the Inverse-Square Law of Gravitation with a Superconducting Torsion Balance

Patrick J. Blackstone<sup>1</sup>, Clive C. Speake<sup>2</sup>, Chris J. Collins<sup>2</sup>

<sup>1</sup>Department of Physics and Astronomy, Bowdoin College  
Brunswick, ME 04011, USA

<sup>2</sup>Department of Astrophysics, University of Birmingham  
Birmingham, B15 2TT United Kingdom

**Abstract.** *A question of increasing interest in gravitational physics examines the validity of the inverse-square law (ISL) of gravity on small scales. Some theoretical models such as the fat graviton and string theory predict that the effect of the fundamental force at sufficiently small range would deviate from the Newtonian prediction. We aim to measure the force of gravity on a scale of  $\approx 15\mu\text{m}$  using a novel superconducting torsion balance. Two major components of this instrument are 1) the ILIAD interferometer to measure rotation in the balance, and 2) the micropositioning system of the source-mass disk, which relies on capacitance measurements in order to align the instrument precisely. This project focused on these two components: aligning the ILIAD and evaluating performance at low ( $N_2$ ) temperatures and numerically evaluating possible deformation patterns in the test masses and the effects of these on capacitance measurements for the micropositioning system.*

## 1. Introduction

[3] gives a good summary of the work done on the ISL violations up through 2009 and, along with 2, provides a description of some of the theories which might imply the existence of such violations. Some such justifications revolve around the dark energy density in the cosmos and identifying a possible characteristic length scale over which gravity may act. Integral to many of these theories is the possibility of extra dimensions, either space or time, which may lead to an increase or decrease in gravitational attraction at small distances respectively. The “fat graviton” theory seeks to solve the cosmological constant problem, claiming that gravitational forces cannot resolve features of the universe below the radius of this force-carrying particle.

Many if not all of these theories seek to replace the inverse-square law with the more general Yukawa potential expression:

$$U = -\frac{Gm_1m_2}{r} (1 + \alpha e^{-r/\lambda})$$

a standard starting point when seeking to analyze new anomalous forces in nature. [3] This potential corresponds to a theory involving a massive graviton where we obtain a characteristic length scale dependent on its mass,  $\lambda = \hbar/mc$ .

The greatest precision that has been achieved in search for violations has been by the Eot-Wash group at the University of Washington who have been using a “negative mass” torsion pendulum shown in Figure 1. Our superconducting torsion pendulum differs from the Eot-Wash group as it will be operating around  $4K$  and rely on the magnetic stiffness of servo coils rather than the harmonic properties of a twisted wire. While the current best results have been taken down to  $55\mu\text{m}$  by Adelberger et al., the Birmingham experiment is expected to reach nominal precision measurements down to approximately  $15\mu\text{m}$ .

While this project does not pertain directly to the detection of gravitational waves or the construction of detectors, as per the theme of this Research Experience, it nevertheless seeks to answer questions fundamental to the work done by groups on GW’s. An understanding of gravitational effects at small distances, at quantum distances, stands as an imposing mystery surrounding the existence and evolution of black holes, one of the primary focuses of GW research. In addition to the advancements which precision measurements of gravity at such small scales could give, the instrumentation utilized and pioneered in this project can be used to achieve likewise unprecedented precision measurements of other interactions acting on small scales, which we mention in Section 6.

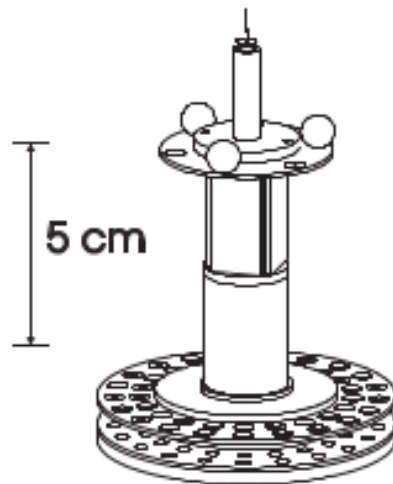


**Figure 1. Diagram of negative mass torsion pendulum used by Adelberger et al. to test ISL violations down to  $55\mu\text{m}$ .**

## **2. Equipment**

Further technical descriptions of the instruments involved in this project can be found in [1], as this report has restricted discussion primarily to those features directly relevant to the work done during the summer.

### **2.1. The Float System**

The float system consists of two parts: the triangular bearing cover and the triangular base with 12 servo coils to provide both upward levitation lift (from the top coils) and stiffness against rotation of the bearing, provided by the side coils. Figure 2 shows a prototype of

the two side by side. The actual bearing is made out of lead to superconduct and repel against the magnetic field generated by the coils at liquid helium temperatures and thus levitating. The disks which comprise the test and source masses will have a periodic density variations as a result of alternating, radial copper and gold strips. The source mass disk will be suspended above the test mass by a micropositioning system which uses capacitance readings to gauge and adjust the gap between the two, and as it is rotated the transverse gravitational attraction between the plates will create a torque on the bearing structure. The ILIAD interferometer (see Section 2.2) will register the displacement and the current in the servo coils along the side will adjust to keep the bearing in place and also betray the magnitude of the torque on the test mass. By tracking the current required to keep the bearing in place as the source mass rotates the strength of the gravitational force between the disks will be recorded.

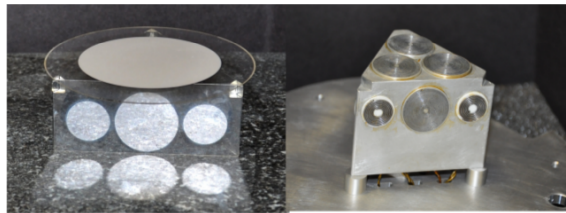


**Figure 2. Prototypes of the test mass and bearing structure to be levitated (left) and the levitation stand with coils (right).**

## **2.2. The ILIAD Interferometer**

ILIAD (Figures 3 and 4) uses a system of beam splitters and cat's eye mirrors to measure the changing distances of the target mirror in Figure 4. In practice, the target mirror is one of the three sides of the float and thus the interferometer will measure any rotational movements in the apparatus, indicating the magnitude of the transverse force acting on the test mass. The ILIAD's integral use of polarizing beam splitters as well as a quarter-wave plate in each of the arms forces only photons of a specific polarization to enter the device and contribute to the output signal. This means that, in the interest of generating as much signal as possible, we must employ a polarization maintaining fiber (see Section 2.3) to guarantee that the polarization of the laser is preserved as it travels from the input, down to liquid helium temperatures, and into the ILIAD.

## **2.3. Polarization Maintaining (PM) Fibers**

There are two standard types of optical fibers designed to maintain the polarization of photons that enter the fiber, shown in Figure 5. We are using a panda style fiber, but the difference between the two is beyond the scope of this report and the general principal is the same. When the acrylic fiber is set around the core and stress rods it creates a bilaterally symmetric stress pattern which transfers into birefringence in the core of the fiber. [4] This creates a "fast" and a "slow" axis along the axes of symmetry of the fiber. These are so called because of the differential effective index of refraction that manifests from this direction-dependent stress gradient. Then any polarization that enters the core of the fiber may be treated as a linear combination of the two preferred axes. Ideally, light which has been aligned with one of the axes does not to "leak" into the orthogonal one, thus maintaining polarization. However, any misalignment causes light to begin

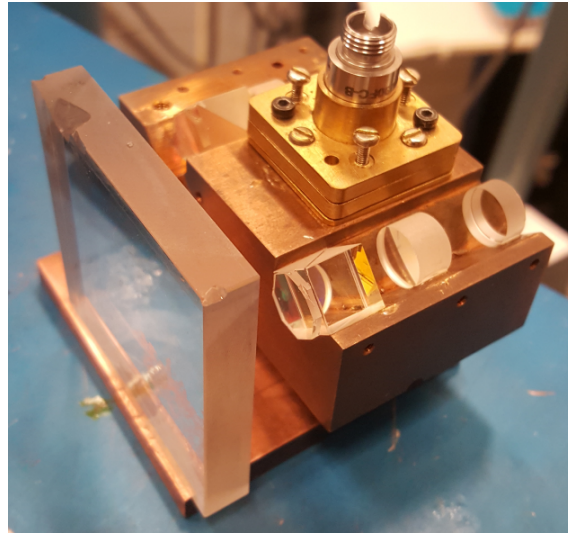


**Figure 3. ILIAD Interferometer**

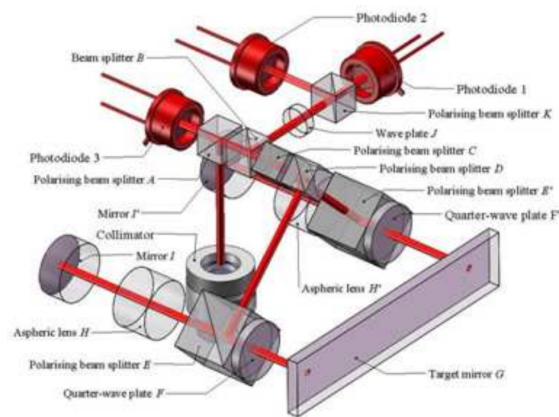


**Figure 4. ILIAD Schematic**

propagating in both axes and so precise alignment is desired for precise polarization. The input end of the fiber may then be rotated as to maximize containment in either axis and to control the polarization which leaves the laser.

### **3. PM Fiber Alignment**

There are a number of degrees of freedom which must be considered in the alignment of the PM fiber in order to 1) maximize the amount of light actually making it into the ILIAD interferometric system and also 2) reduce the beating effects on the intensity of the light exiting the fiber due to changes in temperature of the fiber material. These degrees of freedom are split between the input and output ends, each requiring alignment in their X-Y position, the pitch and yaw of the fiber end, and the angle of the preferred axes with respect to either the polarization of the laser or the ILIAD's primary beam splitting filter.

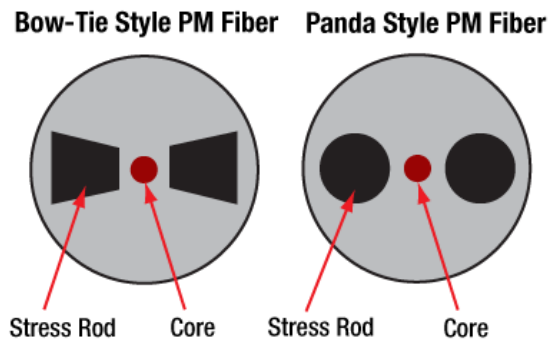


Figure 5. Two schemes for polarization maintaining fibers.

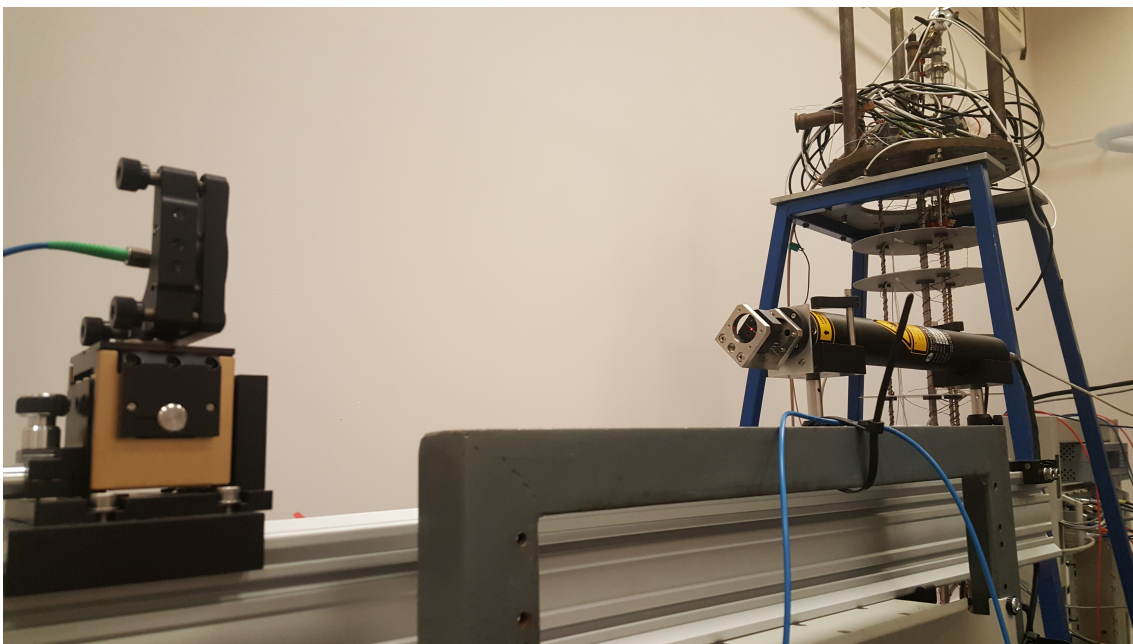


Figure 6. 3 Watt, 633 nm laser mounted on rail pointed towards fiber input.

### 3.1. Thermal Beats within Fiber

As a section of the fiber changes temperature, the stress pattern in the core of the fiber changes in a way such that the speed at which the light moves through either preferred axis varies differently. This results in a beating pattern (illustrated nicely in Figure 10) as the speeds change and the decomposed polarizations of the light slide in and out of phase with each other. This thermal sensitivity is an obvious detriment towards the goal of a stable interferometer reading as the entire experimental setup will be cooled to  $4K$ , and even simply moving my hand too close to the fiber when adjusting the alignment would initiate oscillations due to my body heat.

### 3.2. Input Alignment

In hopes of mitigating this oscillation pattern, the polarization of the laser must approximately match that of one of the preferred axes. The mount into which the input of the laser was mounted included a graduated rotation wheel (Figure 7) which, towards this goal, was used to systematically measure the amplitude of oscillations for a given angle

as a section of fiber was cooled and heated (see Section 3.4). In addition to the preferred axis alignment, the  $x$ ,  $y$ , pitch and yaw could easily be adjusted to scan through the configuration space of the position and direction of the actual tip of the fiber in order to increase output voltage from the photodiode. The laser and input were both mounted on a rail as seen in Figure 6.



**Figure 7. Input of PM fiber with alignment wheel for measuring rotation.**

### **3.3. Beam Splitter and Output Alignment**

The output of the PM fiber is attached to the ILIAD interferometer by the collimator at the top of the instrument in Figure 3. This collimator is mounted on square plates whose planar orientation is controlled and adjusted by the six silver screws around the collimator. In addition, the collimator may rotate freely when not locked into place by the black screws. In this way, the direction and polarization of the output beam can be aligned such that 1) the ILIAD arms can function correctly and measure the displacement of the target mirror and 2) the polarization of the beam closely matches that which is accepted into the interferometer by the initial beam splitting filter. This rotational alignment is important for maximizing the signal from the laser but has the added benefit of further mitigating residual thermal oscillation noise left over from imperfect rotational alignment of the input end of the laser.

### **3.4. Methods of Alignment**

The methods of aligning both input and output ends directionally (i.e. excluding rotation) simply consisted of sequentially adjusting each of 2 or 3 position knobs to a peak voltage, moving on to the next, and cycling through until the signal picked up by the photodiode was adequate. Rotating the input of the fiber required that this process start over again for each angle, so it was impractical and unnecessary to be too precise on this account. The primary challenge of aligning the fiber was the input rotation, for which the photodiode reading needed not be too precise (as long as it was large enough) since it was the ratio of the amplitude of oscillations compared to the size of the original signal that was of interest. We would expect and did observe that this ratio was independent of the original

strength of the signal for a given angle. In order to measure the output intensity of the light through the fiber the output end was mounted to shine through a beam splitter and into the photodiode as seen in Figure 8. This setup was then isolated from the ceiling lights with an opaque cardboard shielding.

In order to align the input of the fiber rotationally we would begin taking data from the photodiode and checked that the signal was stable. Then an open container was partially filled with liquid nitrogen, raised to the level of the rail in Figure 6 and a section of fiber was placed into the container, submerged in the cool air resting above the liquid nitrogen. After a period of time, usually a few minutes, the oscillations would slow as the fiber stopped changing temperature. The fiber would then be removed from the container and an identical beating pattern would start as the fiber began changing temperature again. Both of these features, the phase settling and the second cycle of temperature change, can be seen clearly in Figures 9, 10, and 11. This procedure follows that carried out by the Birmingham group previously, recounted in [4].

Once the data were collected for each angle, the maxima and minima of the most extreme and steadiest oscillations were recorded and an average amplitude was used to calculate the ratio between the oscillations and the steady state voltage.

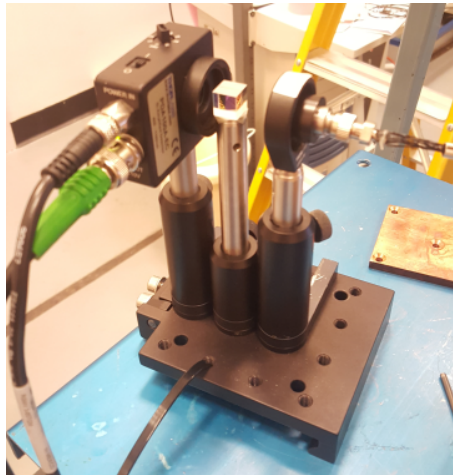


**Figure 8. Mount with photodiode used to measure output intensity of light through fiber.**

### **3.5. Results of Fiber Alignment**

The photodiode data for angles of 40, 65, and 154 are show in Figures 9, 10, and 11 respectively. Figure 12 plots the ratio described above versus the angle read out on the rotation wheel at the input of the fiber. Each data point has a horizontal error bar of  $\pm 2$  based on the graduations of the wheel. The uncertainty in ratio reports 3 times the standard deviation of minima and maxima peak value candidates for each angle.

Where the PM fiber has two preferred axes, would would expect that if either of these were aligned with the polarization of the laser then the oscillations would reduce

to a minimum. Additionally, the two axes ought to be perpendicular to each other and lie 90 degrees apart. Analyzing Figure 12, then, we indeed see two clear valleys in the amplitude of oscillations, the troughs of which indeed lie 90 degrees apart.

In addition to finding the two preferred axes, Figure 12 reveals another interesting feature: the two valleys in oscillation amplitude have significantly different widths as the angle deviates from the minimum. This would indicate that one of the preferred axes is in fact more stable than the other, from which it would follow that photons aligned along the 65 degree axis have a higher likelihood of "leaking" into the axis located around 154 degrees. This more stable axis also seems to have given a greater mitigation of thermal oscillations, although the sharpness of the unstable peak made it difficult to find the true minimum value. In light of this it was clear that the axis at 154 degrees was in fact the best option of alignment. This differs from the strict rectified sine curve found in [4], and further investigation is required into the theoretical justification for this effect.

While the  $x$ ,  $y$ , pitch, yaw alignment of the output was frequently undergone in order to observe the room temperature signal generated by ILIAD, we did not reach a point in the process where it was necessary or feasible to align the rotation angle of the output to match up with the ILIAD interferometer system. However, during preliminary testing of the ILIAD system under vacuum conditions at liquid nitrogen temperature, about 90% of the interference signal was lost. This could indicate internal damage or impurities in the actual fiber itself, possibly necessitating the fabrication of a replacement fiber. Additionally, alternative methods of measuring azimuthal float displacement are being considered, which will be discussed in Section 6.

#### 4. Finite Element Method Magnetics (FEMM)

FEMM is a numerical program used to set up and analyze problems in magnetics, electrostatics, heat flow, and current flow; it can be used for 2-dimensional or axisymmetric schemes. This made it ideal for our purposes where the quantity in mind was the capacitance between two parallel plates under azimuthally consistent deformations. These deformations arise as a function of the circular ring used to hold the test and source foils, which may put strain along the outer edge of the foil during the mounting or cooling processes.

##### 4.1. Model Set up

We see an azimuthal cross-section of the source and test disks in Figure 13, although zoomed into the edge of the disk as to reveal in better detail the tested deformation. In the simulations for this type of deformation, the quantities compared are actually the energies stored in the boundary of the vacuum can which, with an arbitrary potential difference of  $1V$ , is related to the total capacitance by simply

$$E = \frac{1}{2}CV^2 = \frac{C}{2}.$$

The theoretical capacitance for this arrangement can be calculated by

$$C = \int \frac{\epsilon_0 dA}{d(r)}$$

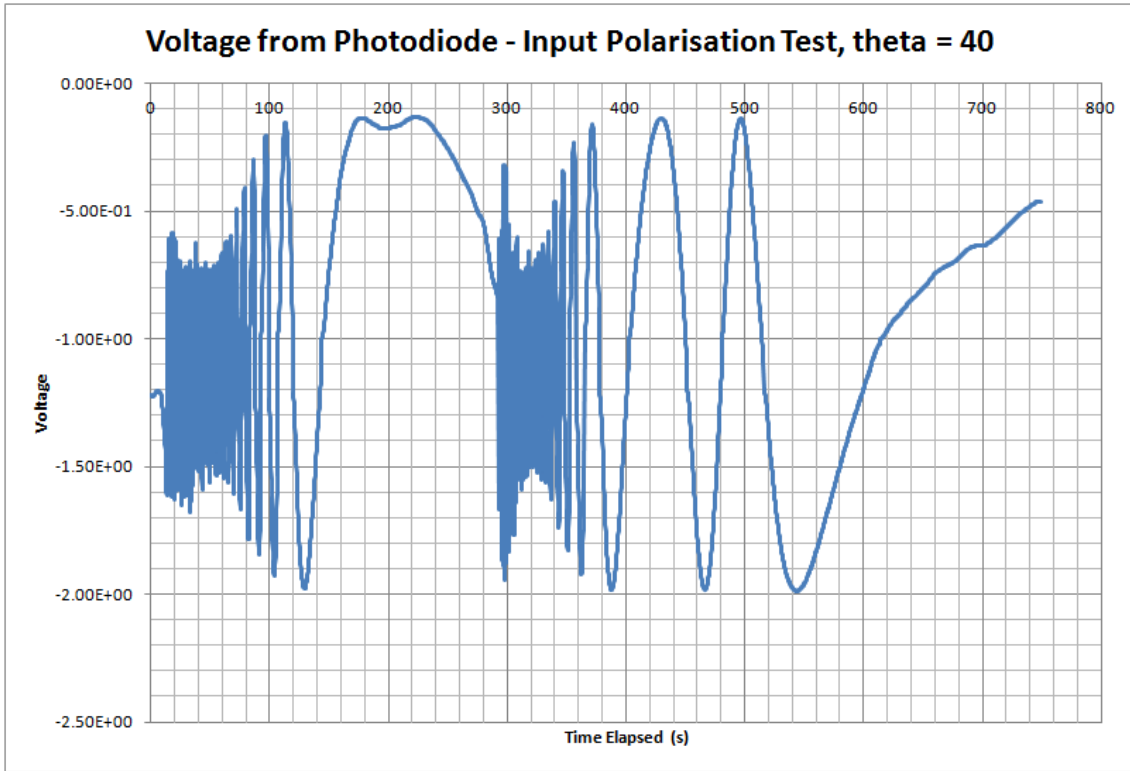


**Figure 9. Photodiode response as a section of the fiber is cooled when input angle is 40 degrees. This is one of the most drastic beating patterns.**

where  $d(r)$  is the distance between the plates as a function of the radius. Let  $a$  be the radius over which the lower plate is flat and  $h$  be the height of the lip. Then for  $0 \leq r \leq a$ ,

$$d(r) = d_0$$

for  $d_0$  the nominal separation. For  $a \leq r \leq R$  (where  $R$  is the total radius of the disk, in this case 40 mm),

$$d(r) = d_0 - \frac{h}{R-a}(r-a)$$

whence

$$\begin{aligned} C &= \frac{\epsilon_0 \cdot (a^2 \pi)}{d_0} + \int_a^b \frac{\epsilon_0 \cdot (2\pi r) dr}{d_0 - \frac{h}{R-a}(r-a)} \\ &= 2\pi\epsilon_0 \left( \frac{a^2}{2d_0} - \frac{R}{h}(R-a + (a + \frac{Rd_0}{h}) \ln(1 + \frac{ah}{Rd_0} - \frac{h}{d_0})) \right). \end{aligned}$$

This analytical result agrees with simple numerical integration for any representative values of all parameters. Further, although this expression is undefined for the case of no lip height,  $h = 0$ , this case is easily integrated as

$$C = \frac{\epsilon_0 A}{d_0} = \frac{\epsilon_0 \pi R^2}{d_0}.$$

Indeed, taking the limit of the general expression for capacitance as  $h \rightarrow 0$  gives the expected expression for two flat plates.

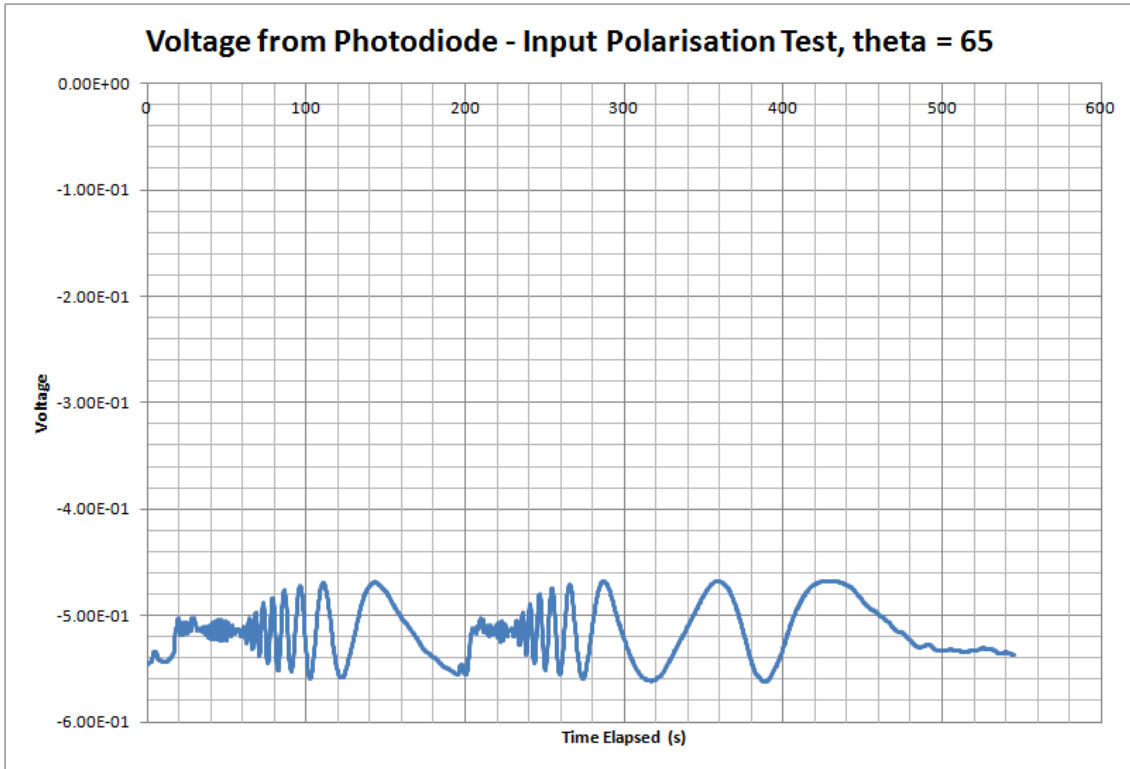


**Figure 10. Photodiode response when input angle is 65. Representative of the unstable minimum region.**

Apart from the two parallel plates in the simulation, there was a need to define a boundary within which the capacitor lay. To this end it was reasonable to encase the plate setup inside of a cylinder, coaxial and positioned at the middle height point as shown in Figure 14. The cylinder, as a boundary condition, was then grounded to the bottom capacitance plate as  $V = 0$  along the top, right, and bottom edges with no condition imposed on the left edge, the axis of the cylinder since there is no physical structure there. This was an appropriate choice of boundary as it reflected the copper vacuum can within which the float structure was to be placed in both dimension as well as potential properties.

One last factor to note about the model is how the energy was calculated. Two different numerical integrations were recorded, so called "unrestricted" and "restricted." Both calculated

$$U = \frac{\epsilon_0}{2} \int \|\mathbf{E}\|^2 dA$$

over different areas. The unrestricted numerical data was acquired by integrating over the entire interior of the vacuum can, while in calculating the restricted energy we integrate only in the area directly between the two plates. It is beneficial to look at both quantities for two reasons. First, we would expect all appreciable contributions to the energy to be in the restricted value, so the difference between the two gives insight as to how much energy is "leaking" out from between the plates into the can. Second, while the total energy of the capacitance may lie in the entire interior of the can, that found within the plates corresponds to the analytical calculation for the energy, as it is this region which was integrated to acquire the previous analytical result. Comparing *these* should give a

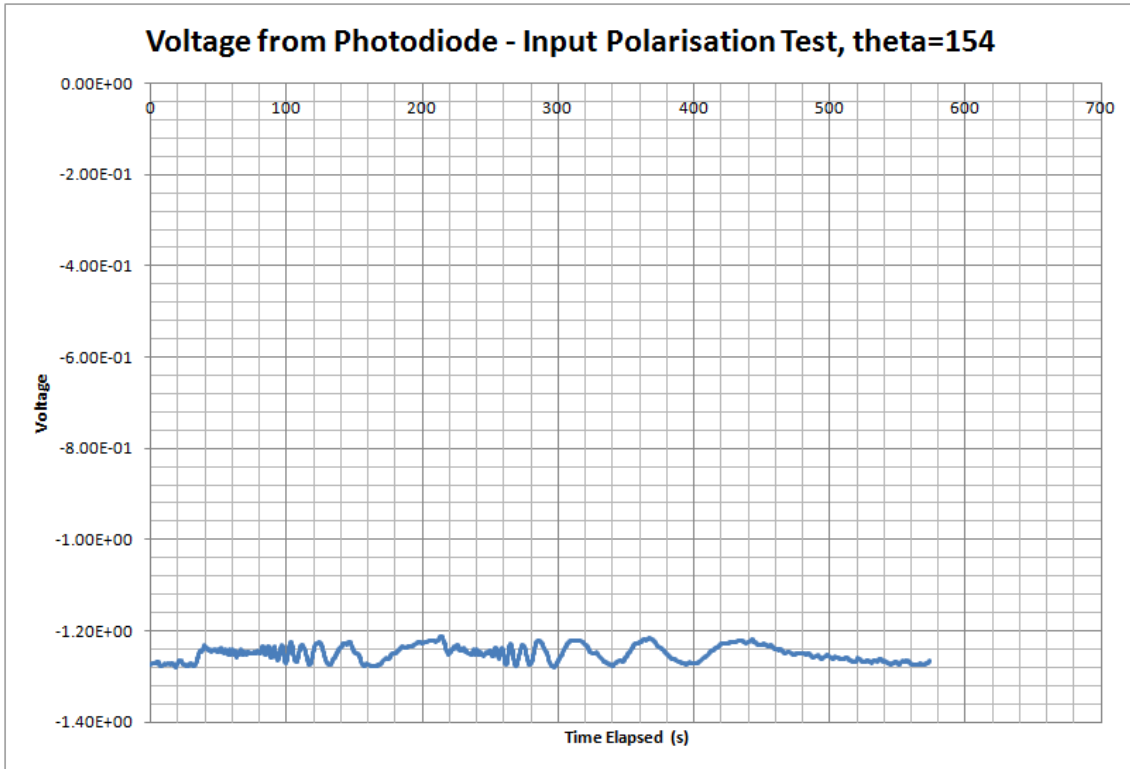


**Figure 11. Response for input angle 154. This is the best sample angle and lies in the more stable region of the ratio curve.**

sense of how correct our analytical result is.

#### **4.2. Results of Calculations**

The data acquired from this simulation through FEMM can be seen in Figure 15. Unfortunately, something is very clearly amiss between the analytical and numerical sets of data. In particular, we would not expect very drastic change in the capacitance between the plates from a slight lip, which is reflected in the analytical value. In Figure 16 we see that the energy increases almost linearly, varying only by a few parts in 100, 000 over the range of interest while our numerical results vary on the scale of parts in 100.

We explored two likely causes of a discrepancy of this magnitude. First, there could have been a unit mismatch as all values input into the FEMM program were in millimeters, while the value for  $\epsilon_0$  was written in units of  $F/m$  when calculating the analytical energy. After thoroughly checking that all parameters were being successfully converted back into meters for this analytical calculation, this source of discrepancy was ruled out. Another possible source of error could be related to the resolution of the mesh with which FEMM analyzed the problem. However, after manually increasing the number of mesh nodes by a factor of 4 there was no noticeable change in the numerical results calculated. A remaining question of veracity in our model could come from fringe effects in the electric field near the edge of the disk, as our analytical integration assumes fieldlines which are precisely parallel to the  $z$ -axis. It remains to take this effect into consideration to determine whether we would expect this fringing effect to cause

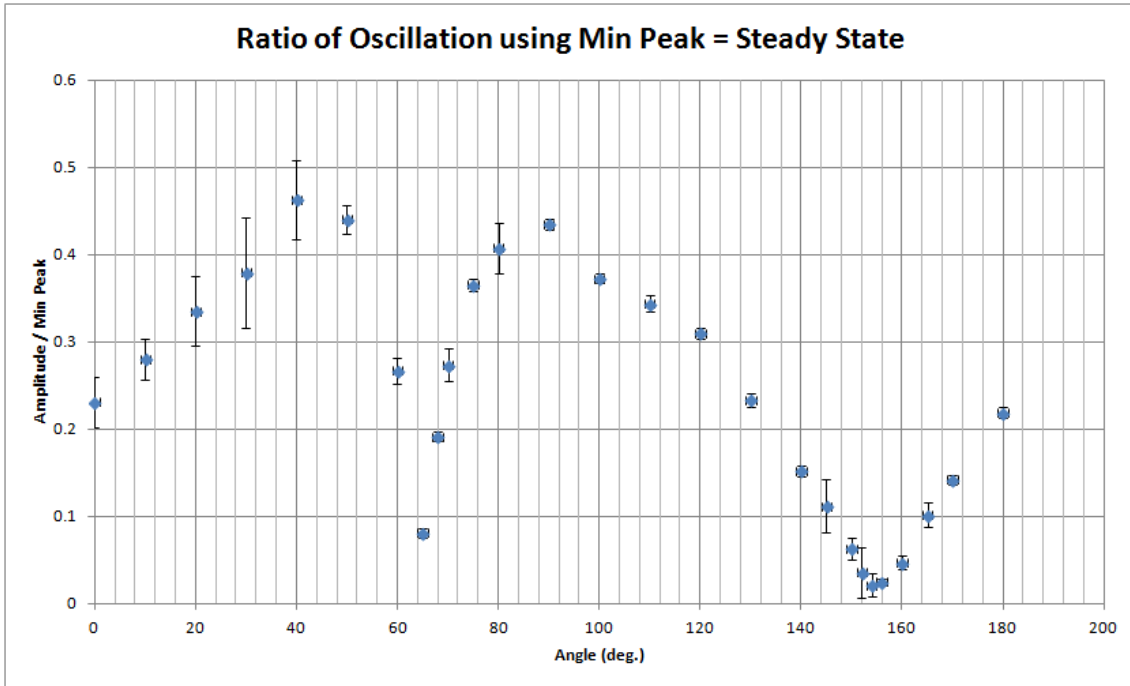


**Figure 12. Graph of ratios as a function of the input angle of the PM fiber. Error bars represent 3 standard deviations in sampling of peaks from photodiode data.**

significant deviation from the current analytical solution.

It is perhaps worth noting that the restricted numerical data and the analytical data are equal for a lip height of  $h = 0$ , as we would surely expect. This perhaps lends credence to the hypothesis that fieldline fringe effects are causing significant error, for in the case of a flat disk the electric field within the restricted area would exhibit almost no change in direction moving from one plate to another. This is apparent as the plane of both disks at the edge in the case of  $h = 0$  is parallel to the  $z$ -axis and so field lines must exit the top and enter the bottom plate pointing in the  $z$  direction. This is opposed to the case of a nonzero lip, where the field lines indeed *must* rotate in order to enter the bottom plate normal to the surface, as is evident in Figure 13.

The source of this error is yet to be made clear. However, field line directionality is a strong candidate which will not be too difficult to check moving forward. Once the numerical and analytical data align, this script may be used in conjunction with precision scanning instruments (to describe deformations) to assist the micropositioning system in its goal of recording and adjusting the spacing and angle between the two plates.

## 5. Conclusions

The input of the fiber was successfully rotationally rotated, and the data acquired therein gleaned insight and credence to the apparent stability preference between the two preferred axes of the PM fiber. The work done this summer also honed the technique and process for actually aligning the angle of the input of the fiber. Unfortunately, this particular fiber has not yet proved able to transmit enough light into the interferometer

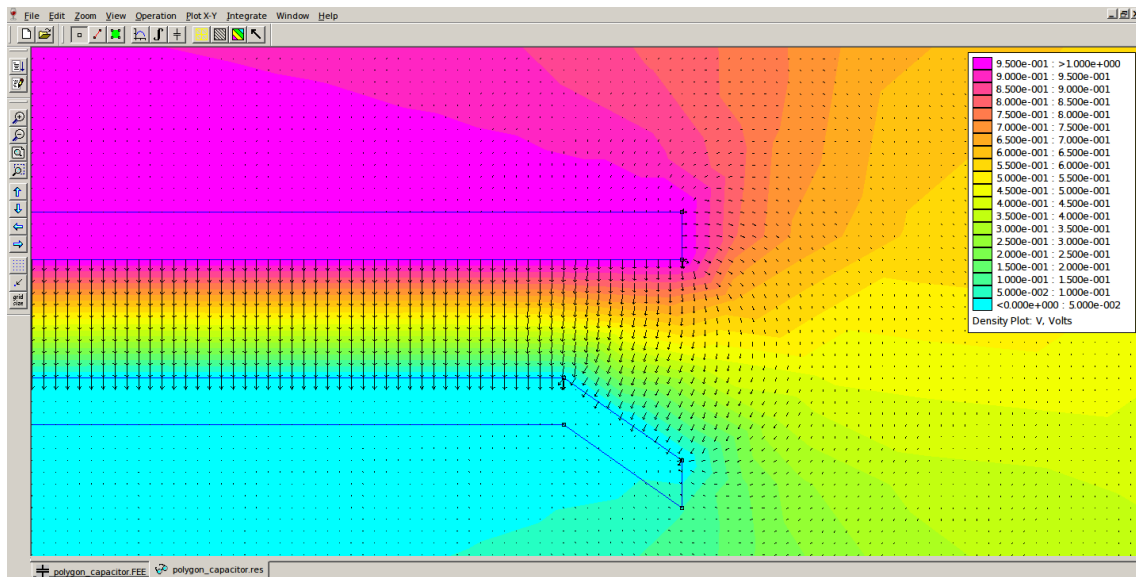


**Figure 13. FEMM analysis for a gap of 100um.**

at nitrogen temperature, and so either another fiber is required or a new approach to measuring rotation in the float.

Additionally, although the FEMM script was successful at constructing and editing the deformation scheme of primary interest this summer, the data taken from this do not immediately agree with analytical predictions of the energy stored between the capacitors. This may, however, demonstrate a previously unthought necessity to consider radial components of the electric field between plates when predicting capacitance between various configurations.

The experimental set up is not yet ready to begin measuring gravity on the scale desired but significant steps were made this summer towards understanding the obstacles and nuances ahead of us.

## **6. Further Work**

Where the use of a PM fiber and the ILIAD interferometer has been met with consistent difficulties and set backs, it may be necessary to continue exploring alternative methods of measuring azimuthal displacement of the test disk. In particular, there is promise in measuring how the capacitance between the float structure and a stationary plate change, betraying movement and thus allowing for appropriate adjustments in the currents of the side coils of the float system.

With a working displacement measurement system the experimental setup may be used with other float disks designed to evaluate other transverse force effects. Most notably, the Casimir force can be measured by using two homogeneous disks with heavily exaggerated strip topography. Such an observation of the Casimir force could stand as a landmark precision measurement if measured alongside the design sensitivity of the

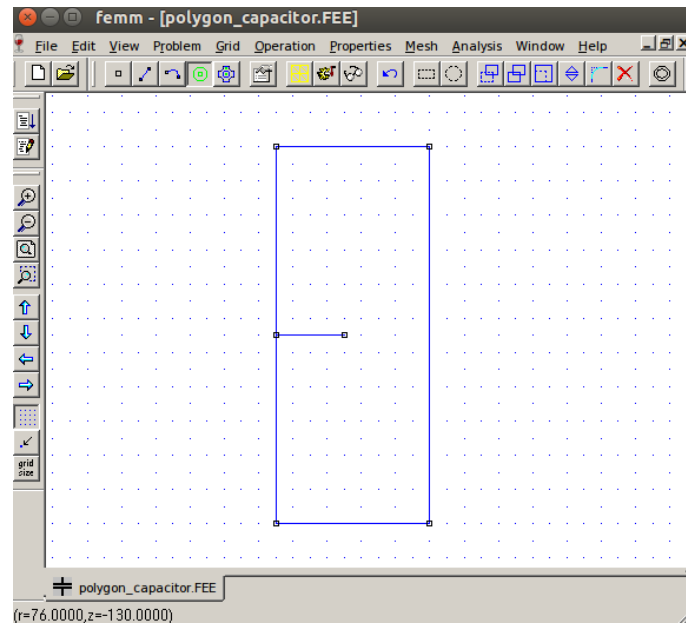


**Figure 14. Diagram of region to be integrated. Vacuum can has the same dimensions as the real can: a radius of 90mm and a height of 220mm, centered on the  $z=0$  plane. The axis of rotation,  $r=0$ , is along the left edge of the rectangle.**

torsion balance.

## 7. Acknowledgements

I would like to thank the NSF for funding this international Research Experience and the University of Florida for coordinating and facilitating it. The Department of Astrophysics at the University of Birmingham was very welcoming through the summer and my advisers, Clive Speake and Chris Collins, acted as tireless troves of information and inspiration.

## 8. References

- [1] C. C. Speake et al. Documentation for STFC Oversight committee. Technical report, University of Birmingham, 2011.
- [2] E.G. Adelberger, B.R. Heckel, A.E. Nelson, *Ann. Rev. Nucl. Part. Sci.* 53 77, (2003)
- [3] R. D. Newman, E. C. Berg, and P. E. Boynton, *Space Sci. Rev.* 148, 175 (2009) [4] C. C. Speake et al. A cryogenic optical feedthrough using polarization maintaining fibers. *Rev. Sci. Instrum.* 87, 033111 (2016)

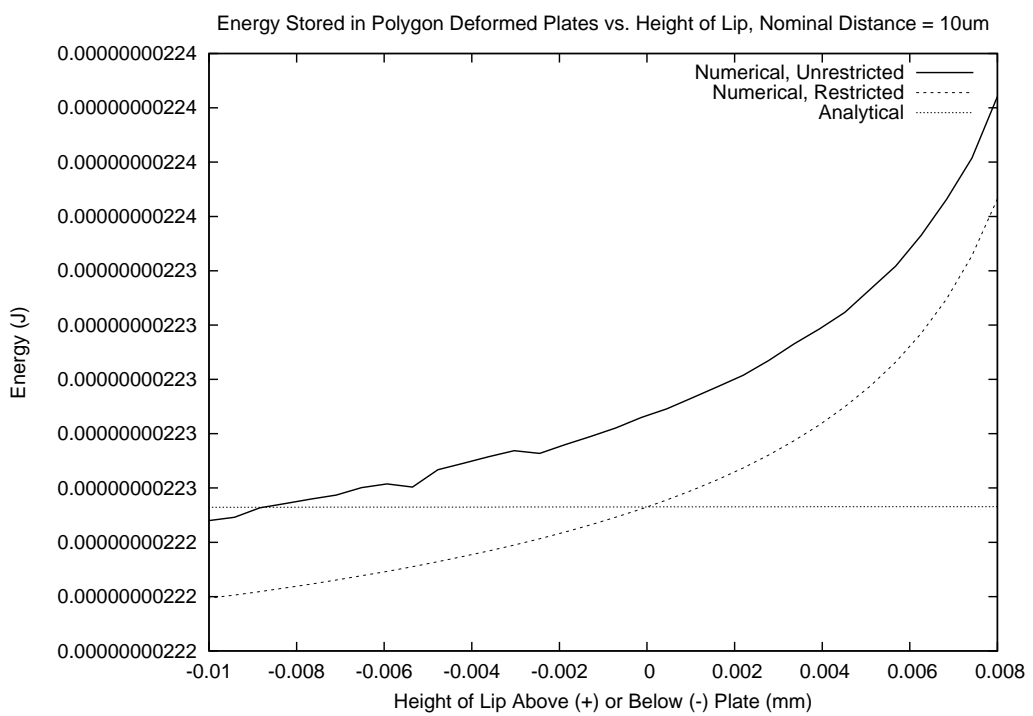


**Figure 15. Plot showing Numerical and Analytical calculations of energy stored in the plates at a potential difference of 1V. Here, the nominal distance between plates is 10um.**

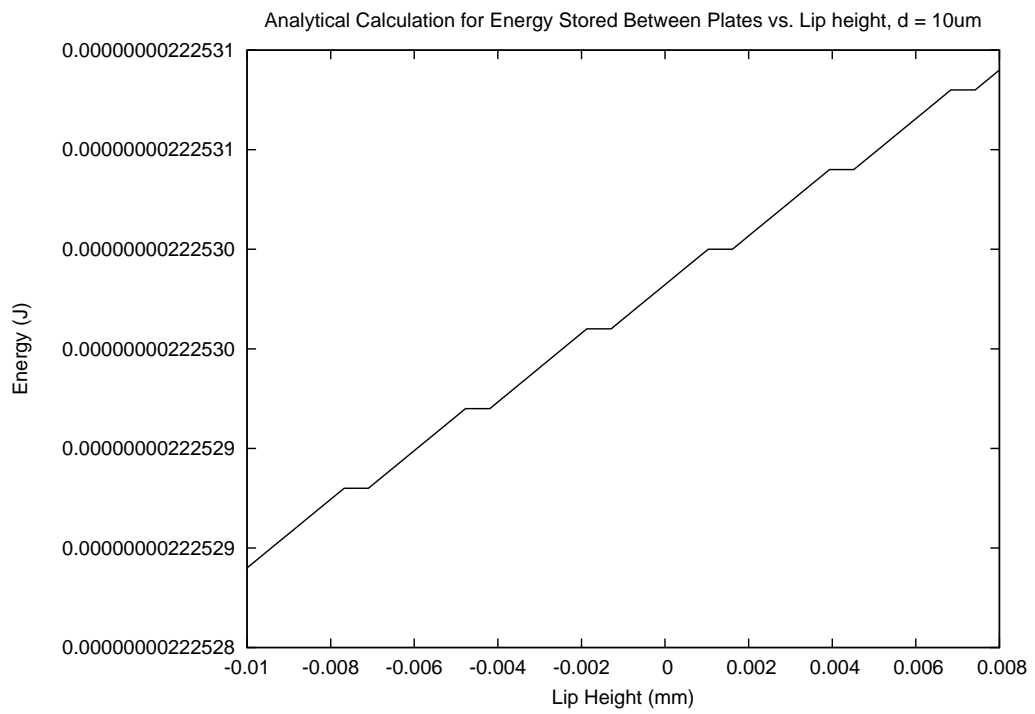


**Figure 16. Same data as in Figure 15, rescaled to show only analytical data and how it varies.**